Available online at www.sciencedirect.com

ScienceDirect

Procedia CIRP 111 (2022) 105–110

www.elsevier.com/locate/procedia

12th CIRP Conference on Photonic Technologies [LANE 2022], 4-8 September 2022, Fürth, Germany

Structural deviations of bulk metallic glasses in downfacing surfaces fabricated via Laser Powder Bed Fusion

Jan Wegner[a,*], James P. Best[b], Norman Schnell[a], Stefan Kleszczynski[a,c]

[a] University of Duisburg-Essen, Lotharstrasse 1, 47057 Duisburg, Germany
[b] Max-Planck-Institut für Eisenforschung GmbH, Max-Planck-Str. 1, 40237 Düsseldorf, Germany
[c] Center for Nanointegration Duisburg- Essen (CENIDE), Carl-Benz-Str. 199, 47057 Duisburg, Germany

* Corresponding author. Tel.: +49 2033793075; *E-mail address:* jan.wegner@uni-due.de

Abstract

Laser powder bed fusion is an established and viable method to produce large and complex bulk metallic glass geometries. However, the thermal gradients and cooling rates during processing are affected by geometric features, in particular close to the part-powder bed interface, which may impair vitrification and mechanical properties. As such, the present contribution aims towards a better understanding of laser-processing and the resulting properties in overhanging structures. Density measurements revealed a distinct impact of the elevation angle on the densification accounting for up to 5% relative density. Finite element simulations suggest this is attributed to increased peak temperatures and reduced heat flow at the part-powder bed interface. However, microhardness and nanoindentation measurements of samples processed under optimized energy density close the interface revealed a minor impact of the altered thermal history on the mechanical properties under the examined conditions.

Keywords: Bulk metallic glass; Laser powder bed fusion; Downskin; Overhang; Microhardness; Nanoindentation

1. Introduction

Additive manufacturing of bulk metallic glasses (BMGs) through laser powder bed fusion of metals (PBF-LB/M) constitutes a synergetic approach to exploit the transient laser-material interaction for the creation of advanced materials. BMGs offer an outstanding combination of high strength and elastic limit, making them excellent options for structural material applications [1]. However, vitrification requires rapid quenching from the molten state, which *de facto* restricts the size and complexity of conventional processing techniques such as casting. First introduced by Pauly et al. for a Fe-based alloy [2], various glass-forming compositions have since then been investigated using the PBF-LB/M process [3,4].

Among these, Zr-based BMGs feature a favorable combination of fracture toughness and glass-forming ability (GFA) for utilization in PBF-LB/M. In particular, AMLOY-ZR01 (tradename, formerly AMZ4) has received attention due to its commercial availability through Heraeus AMLOY Technologies GmbH. Several studies have reported its processability [5–7] and resulting mechanical properties [8–12]. PBF-LB/M manufactured AMLOY-ZR01 reaches flexural strengths up to 2.1 GPa and elastic limits of 2-3 % leading to a very large modulus of resilience, especially in comparison to crystalline alloys such as Ti6Al4V [13].

However, structural integrity is often challenged by residual porosity and nano-crystallization based on the applied processing parameters [14]. Both are accompanied by a reduction of the desirable mechanical properties, such as fracture toughness [12] and flexural strength [6]. Although the cooling rates associated with the laser-material interaction during PBF-LB/M (5×10^5 K/s) are far beyond the critical cooling rates reported for cast AMLOY-ZR01 (20 K/s), CuZrO and CuZr phases are frequently observed in the laser-processed

10.1016/j.procir.2022.08.147

material [14–16], with GFA and CuZrO nucleation linked to elevated oxygen contamination present in powder materials [6,9,15,16]. These intermetallic phases are reported to embrittle and weaken the material [3,9,17]. BMG parts thus require a careful selection of process parameters to ensure amorphous solidification and sufficient densification. From Oliveira et al. [18], dense fabrication is limited by keyhole porosity at high energy input and lack-of-fusion (LOF) at low energy input. For BMGs, this range is further restricted by (nano)crystallization accompanied with increasing energy density (see Fig. 1).

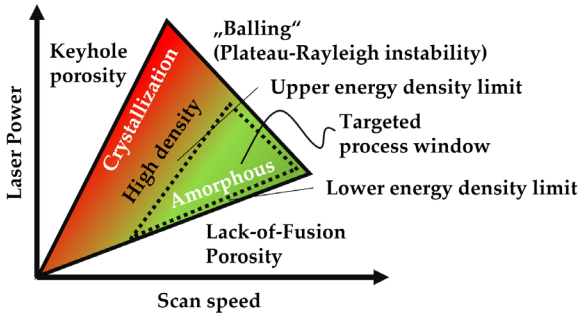

Fig. 1. Illustration of the resulting parameter window for amorphous and dense processing of BMGs in PBF-LB/M. Inspired by Ref [17].

Further, variations in thermal history and local chemistry of PBF-LB/M manufactured parts can be linked to significant variations of atomic-scale ordering, generally expressed through the short- and medium-range order [19]. Changes in the atomic-scale order affect the mechanical response of the glass through variation in e.g. local symmetries such as for crystal-like or icosahedral formations [20,21].

This sensitivity towards the thermal history during processing raises the question of which secondary factors besides the applied process parameters may lead to the formation of crystalline defects and structural variations of the amorphous phase. PBF-LB/M is well known for enabling the fabrication of complex structures and lattices. However, such geometric features exhibit a different thermal history to that of the bulk. Areas with increased powder bed interface are prone to overheating. The thermal conductivity of metal powders for PBF-LB/M is only a fraction of that of the bulk material due to the low conductivity of infiltrated gases [22,23]. This eventually obstructs the heat flow, which can lead to overheated regions, for instance in overhanging areas. In crystalline alloys, this phenomenon is often associated with dross formation, surface roughness, dimensional inaccuracy, and residual stresses [24–26]. Hooper investigated the temperature profiles of Ti6Al4V in Ref. [27] and found a drop in the peak temperature gradients from 20 K/µm to 10 K/µm in overhanging geometries.

In view of BMG fabrication via PBF-LB/M, this raises the hypothesis that the applied process parameters need to be adapted in overhanging areas to counteract the reduced cooling rates. The present work investigates the interplay between different overhanging angles, the applicable process parameters, the spatial thermal gradients, the cooling rate (dT/dt), and the resulting mechanical properties.

2. Experimental procedure

Gas atomized AMLOY-ZR01 powder with nominal composition $Zr_{59.3}Cu_{28.8}Al_{10.4}Nb_{1.5}$ (in at.-%) was provided by Heraeus AMLOY Technologies GmbH. The powder has a mean particle diameter d_{50} of 23.7 µm and a comparatively high oxygen content of ~2300 µg/g [6]. Sample manufacturing was conducted on the commercial EOS M100 PBF-LB/M system (eos GmbH, Germany) equipped with a 200 W fiber laser with a nominal focus diameter of 40 µm [28]. To evaluate the impact of the overhanging angle, parallelepiped samples with an edge length of 5 mm were built, ensuring equivalent exposure areas and interlayer times during the process.

Fig. 2 displays the processed sample geometries and the nominal geometrical features of the overhanging area. The nominal unsupported length x increases with the tangent of the elevation angle α from 5.4 µm to 20 µm.

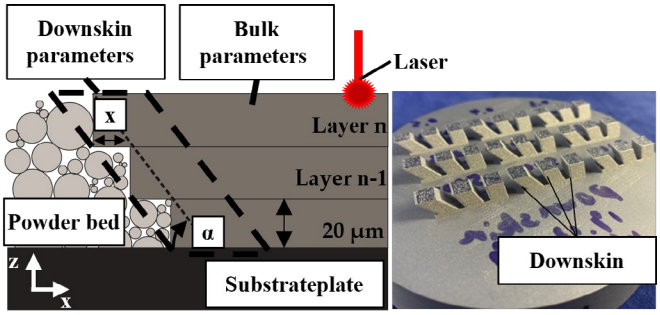

Fig. 2. Left: Schematic illustration of the overhanging length x based on the elevation angle α during PBF LB/M. Right: PBF-LB/M samples fabricated for investigation.

Three elevation angles α of 45°, 60°, and 75° were investigated (see Fig. 2). Each angle was processed under each parameter set in the downskin region as listed in Table A of the appendix. The local parameter adjustment was applied for the first 0.4 mm from the edge. Bidirectional scan paths were oriented parallel to the contour in the y-direction. The corresponding scan speed was varied in four steps from 2000-5000 mm/s resulting in nominal volume energy densities (E_v) of 10-25 J/mm³ (see Table A). For the material bulk, an E_v of 25 J/mm³ was used. Relative density was assessed by optical microscopy of microsections. Samples were cut along the Z-X plane (as defined in Fig. 2), ground, and polished. Microscopy was conducted using an Olympus BX51M device.

Additionally, a qualitative mesoscopic FEM simulation of the time-temperature relation was conducted using COMSOL Multiphysics 6.0. Therefore, the boundary conditions of the experiments (process parameters, scanning strategy, and geometry) were transferred to a 1 mm² section of the sample geometry. Due to the challenges of validation and verification in the determination of true temperatures in FEM models, temperatures were normalized to 1 and qualitatively compared. The thermophysical values and the meshing used for the simulation are given in Table B of the appendix. Assumptions for heat losses due to convection and radiation are based on the work of Schnell et al. [29]. Due to a lack of data, the heat conductivity of the surrounding powder bed was set to 0.26 W/m K based on results for Ti6Al4V in Ref. [22].

Microhardness measurements were performed using a Leco machine at HV0.1 on the cross-section of fabricated samples embedded in resin. For each sample, grids of 5 × 10 were performed with the left-hand edge of the grid starting ca. 50 µm from the sample edge (see Fig. 6a). Approx. 80 µm spacing was used between indents. For nanoindentation, two grids each containing 30 indents were placed totally within the downskin zone, starting ~50 µm from the surface. A Hysitron Triboindenter was used for the measurements, with a diamond Berkovich tip in quasi-displacement control and an indentation set-point of 300 nm. Loading was achieved over 20 s, followed by a 5 s hold before unloading. A spacing of 15 µm was used between indents.

3. Results and discussion

3.1. PBF-LB/M processing – densification

Given the anticipated impact of the overhanging angles on reducing the cooling rate, the applied E_v in the downskin-region was incrementally reduced to determine the minimal energy input to achieve satisfactory densification. A relative density of 99.5% ± 0.1 in the sample bulk was achieved for the reference processing parameters of 40 W and 2000 mm/s (taken from [6]), which is in good agreement with previous studies [6,17]. X-ray diffraction of a bulk sample indicates an amorphous state, within the detection limits of the technique, as shown in Fig. A of the appendix.

Fig. 3 displays an exemplarily microsection for downskin areas with different elevation angles processed with 15 J/mm³. Here, the E_v of the overhanging area is reduced by 40% compared to the bulk material (25 J/mm³).

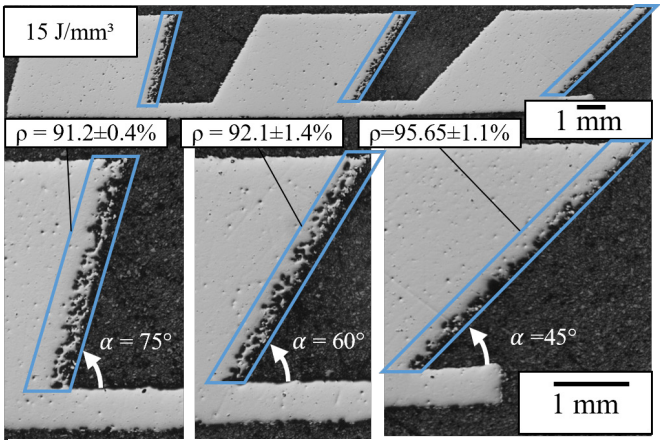

Fig. 3. Microsection displaying the impact of the overhanging angle on densification within the downskin area. The material bulk was processed with 40 W and 2000 mm/s (25 J/mm³). Downfacing surfaces were processed with an increased scan speed of 3333 mm/s (15 J/mm³).

The adjustment leads to irregularly shaped voids indicating LOF-porosity; associated with insufficient energy density [18]. The increasing scan speeds investigated in this study decrease the dwell time of the melt pools. This leaves insufficient time to fill the voids and fully consolidate the powder material [30]. Interestingly, densification also appears to be a function of the elevation angle α. It gradually increases from 91.02% ± 0.4 for α = 75°, to 95.65% ± 1.1 for α = 45°. In this context, the impact of the elevation angle on the thermal history was assessed by a simple mesoscopic FEM simulation.

The heat flow resulting from a Gaussian laser source moves along an individual scan vector parallel to the sample contour, with an offset of one hatch distance (0.04 mm) towards the bulk material. The parameters for the simulation correspond to the settings given in Table A for an E_v of 20 J/mm³ (40 W and 2500 mm/s). Thermophysical properties and boundary conditions were set according to Table B of the appendix. The determination of absolute peak temperatures during the PBF-LB/M process through numerical simulation incurs large uncertainties and strongly depends on comprehensive calibration and validation of the model [29]. For the sake of simplicity, the calculated results are displayed normalized on the maximum temperature computed throughout the study. Fig. 4 depicts the time-temperature curves of the investigated elevation angles α in the center of the scan line.

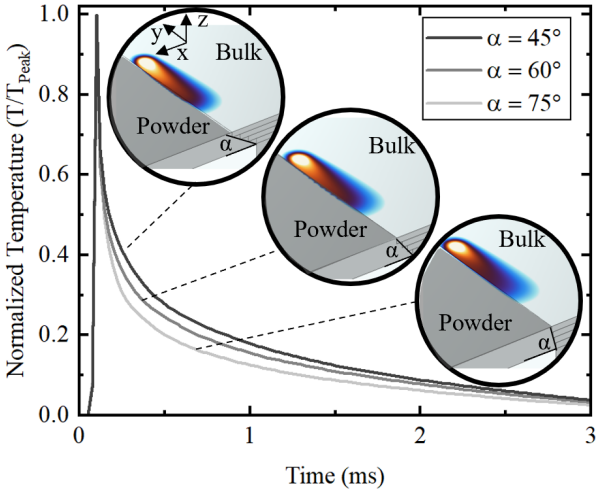

Fig. 4. Time-temperature curve of a single scan line along the downskin region (0.02 mm away from the contour). The spatial heat distribution on the is indicated by surface plots for the respective angles.

The numerical approximation reveals a slight increase in the peak temperature of ~5% from 75° to 45° elevation angle. The localized cooling rate (dT/dt) of a point situated 0.04 mm away from the part-powder bed interface is directly proportional to the elevation angle. This is caused by the significantly lower heat conductivity of the surrounding powder bed in comparison to the bulk [22,31]. With decreasing elevation angle, the surface area for conductive heat removal through the part itself is reduced, affecting thermal gradients in the HAZ (Fig. 4). For an angle of 75°, the temperature field is nearly symmetrical and broadly unaffected by the interface layer. At lower angles, the high-temperature contours (displayed in orange) enlarge and shift towards the powder interface, indicating heat accumulation. These findings support the observation made for the densification behavior of the different elevation angles in Fig. 3. The insulating effect of the powder material and reduced heat flow in the downskin region leads to local heat accumulation, which increases the peak temperatures and reduces the cooling rate. Thus, longer dwell times and larger melt pools lead to the higher densification observed in Fig 3.

Fig. 5 summarizes the relative density in the downskin area based on the elevation angle α and the applied E_v. Naturally, the porosity increases with decreasing volume energy density

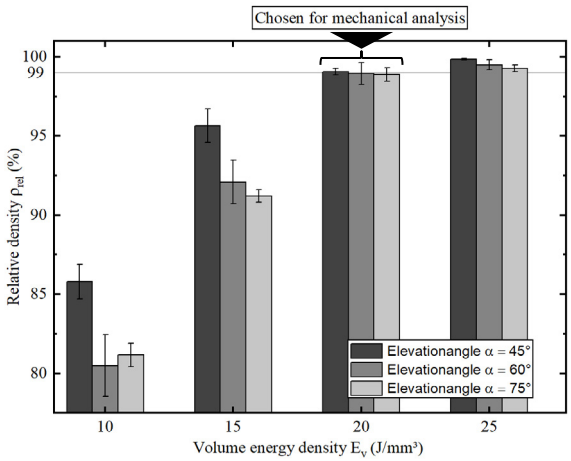

Fig. 5. Influence of the overhanging angle and the applied E_v on densification within the downskin area.

E_v. However, the impact of the elevation angle on densification discussed earlier partly counteracts the LOF-porosity.
Samples with an elevation angle α of 45° generally show the highest densification at any given E_v. Except for an E_v of 10 J/mm³, the density gradually decreases with increasing elevation angle. However, densification below 99% is not acceptable for structural applications. An E_v of 20 J/mm³ was found suitable for high densification while reducing the thermal load, associated with crystallization in BMGs and potential loss of their desirable mechanical properties [6,12]. As such, this parameter set was selected for an evaluation of the mechanical properties.

3.2. Mechanical properties

Considering the impact of the elevation angle on the thermal history and densification, microhardness testing was first performed over the downskin region. Fig. 6a, b illustrates microhardness maps for the three different elevation angles processed with 20 J/mm³ in the downskin. The microhardness was found to be 512 ± 17 HV (45°), 507 ± 16 HV (60°), 502 ± 20 HV (75°), corresponding well to other laser-processed studies of the same alloy [19]. A perceptible decrease of the HV was observed in the downskin region compared to the bulk, which could be reasoned by the decreased energy density in the downskin, however differences as a function of elevation angle are within a standard deviation.

Nanoindentation measurements performed on all three samples entirely within the downskin region highlighted that no large variation existed within this region, and also between samples with varying elevation angle. Mean values for the nanoindentation hardness (H) and reduced modulus (E_R) were found to be within a single standard deviation (1σ) for all three samples. Of note, the 45° sample showed a broader distribution (larger standard deviation) in both hardness and modulus (Fig. 6c).

For an elevation angle of 45° values of H 6.0 ± 0.6 GPa and E_R 99 ± 4 GPa were obtained, in comparison to H 6.1 ± 0.3 GPa and E_R 101 ± 2 GPa (60°) and H 6.1 ± 0.3 GPa and E_R 100 ± 2 GPa (75°). For all values the mean ± 1σ is presented. While the values are consistent, the larger scatter for 45° may be explained by the presence of a more heterogeneous structure caused by the slower temperature decay evidenced in Fig. 4. However, it must be reinforced that such differences are minor at the studied elevation angles.

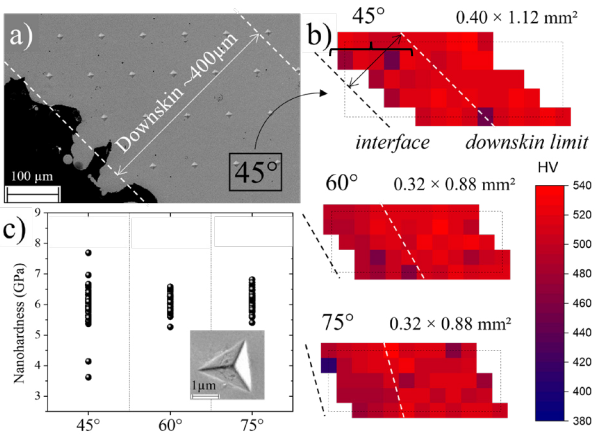

Fig. 6. a) Micrograph of microhardness grid in the downskin region at an elevation angle α of 45°. b) Heat map of the microhardness measurements for the investigated elevation angles. c) Nanohardness distributions based on the elevation angles (inset SEM image of residual nanoindent).

4. Conclusion

The impact of different elevation angles and process parameters on the near-surface densification during PBF-LB/M of a Zr-based BMG was investigated. The impact of varying thermal history on the mechanical properties were further studied through local indentation for sample processed at 20 J/mm³ in the downskin area. The findings can be summarized as:

- The elevation angle impacts the densification in the downskin area. Larger overhangs lead to higher density, especially if a low E_v is applied. Here, the porosity decreases ~5–9% based on the applied E_v and elevation angle.
- FEM simulations link densification increases for larger overhangs to increased peak temperatures and reduced cooling rates.
- The elevation angle imparts only a minor impact on the mechanical properties of the amorphous structure for the investigated E_v. The results indicate sufficient thermal stability of AMLOY-ZR01 to resist lowered cooling rates in the overhanging structures.
- Increased scatter in the nanohardness with 45° elevation angle implies minor increased structural heterogeneity of the most strongly overhanging structure.

Finally, the results confirm the good aptitude of Zr-based BMGs for PBF-LB/M due to their high thermal stability. However, only large overhanging angles were here investigated. Other geometries that feature further reduced heat dissipation might be more sensitive for the fabrication of BMGs. The observed heterogeneity fingerprints in the nanohardness, together with the numerical analysis in Fig. 5, forecast that a more sophisticated parameter optimization might be required in view of complex BMG parts with larger overhanging areas and unfavorable aspect ratios.

Acknowledgements

The authors want to thank Wentao Wang for the diligent support in the laboratory. Further we acknowledge the fruitful discussions and support for the FEM simulation of Simon Preuss. Heidi Bögershausen and Leon Christiansen at MPIE are also thanked for support in sample preparation, mechanical testing and SEM imaging. This research was funded by German Federal Ministry for Economic Affairs and Energy (BMWi), grant number 19927N and 21227N. The APC was funded by the Open Access Publication Fund of the University of Duisburg-Essen.

5. Appendices

Table A. Applied processing parameters and resulting volume energy density E_v in the downskin area.

Laser Power (W)	Hatch Distance (mm)	Scan speed (mm/s)	Volume energy density (J/mm³)
40	0.04	2000	25 (reference)
		2500	20
		3333	15
		5000	10

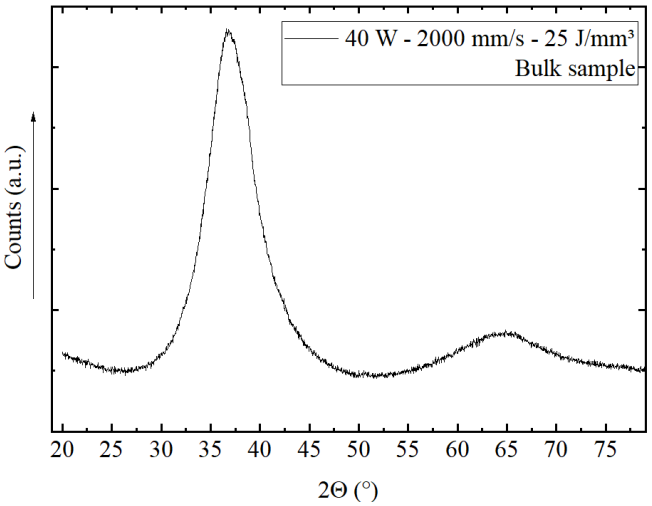

Fig. 7. XRD diffractogram of a PBF-LB/M AMZ4 cubic sample processed with 25 J/mm³ (40 W – 2000 mm/s).

Table B. Properties used for the FEM simulation.

Parameter	Value	Reference
ρ [kg/m³]	6616	[32]
l_{bulk} [W/m K]	5-16	Determined by laser flash meas.
l_{powder} [W/m K]	0.26	[22]
c_p [J/mol K]	$3*8.314 + 5.224*10^{-4}*T + 1.037*10^{7}*(T^{-2})$	[33]
Absorptivity [-]	0.3	[33]

6. References

[1] M. Telford, The case for bulk metallic glass, Materials Today 7 (2004) 36–43. https://doi.org/10.1016/S1369-7021(04)00124-5.
[2] S. Pauly, L. Löber, R. Petters, M. Stoica, S. Scudino, U. Kühn, J. Eckert, Processing metallic glasses by selective laser melting, Materials Today 16 (2013) 37–41. https://doi.org/10.1016/j.mattod.2013.01.018.
[3] N. Sohrabi, J. Jhabvala, R.E. Logé, Additive Manufacturing of Bulk Metallic Glasses—Process, Challenges and Properties: A Review, Metals 11 (2021) 1279. https://doi.org/10.3390/met11081279.
[4] P. Zhang, J. Tan, Y. Tian, H. Yan, Z. Yu, Research progress on selective laser melting (SLM) of bulk metallic glasses (BMGs): a review, The International Journal of Advanced Manufacturing Technology (2021). https://doi.org/10.1007/s00170-021-07990-8.
[5] J. Wegner, M. Frey, S. Kleszczynski, R. Busch, G. Witt, Influence of process gas during powder bed fusion with laser beam of Zr-based bulk metallic glasses, Procedia CIRP 94 (2020) 205–210. https://doi.org/10.1016/j.procir.2020.09.039.
[6] J. Wegner, M. Frey, M. Piechotta, N. Neuber, B. Adam, S. Platt, L. Ruschel, N. Schnell, S.S. Riegler, H.-R. Jiang, G. Witt, R. Busch, S. Kleszczynski, Influence of powder characteristics on the structural and the mechanical properties of additively manufactured Zr-based bulk metallic glass, Materials & Design 209 (2021) 109976. https://doi.org/10.1016/j.matdes.2021.109976.
[7] J.J. Marattukalam, V. Pacheco, D. Karlsson, L. Riekehr, J. Lindwall, F. Forsberg, U. Jansson, M. Sahlberg, B. Hjörvarsson, Development of process parameters for selective laser melting of a Zr-based bulk metallic glass, Additive Manufacturing 33 (2020) 101124. https://doi.org/10.1016/j.addma.2020.101124.
[8] J. Wegner, M. Frey, P. Stiglmair, S. Kleszczynski, G. Witt, R. Busch, Mechanical properties of honeycomb structured Zr-based bulk metallic glass specimens fabricated by laser powder bed fusion, sajie 30 (2019). https://doi.org/10.7166/30-3-2265.
[9] P. Bordeenithikasem, M. Stolpe, A. Elsen, D.C. Hofmann, Glass forming ability, flexural strength, and wear properties of additively manufactured Zr-based bulk metallic glasses produced through laser powder bed fusion, Additive Manufacturing 21 (2018) 312–317. https://doi.org/10.1016/j.addma.2018.03.023.
[10] N. Sohrabi, M. Hamidi-Nasab, B. Rouxel, J. Jhabvala, A. Parrilli, M. Vedani, R.E. Logé, Fatigue Performance of an Additively Manufactured Zr-Based Bulk Metallic Glass and the Effect of Post-Processing, Metals 11 (2021) 1064. https://doi.org/10.3390/met11071064.
[11] N. Sohrabi, J. Jhabvala, G. Kurtuldu, M. Stoica, A. Parrilli, S. Berns, E. Polatidis, S. van Petegem, S. Hugon, A. Neels, J.F. Löffler, R.E. Logé, Characterization, mechanical properties and dimensional accuracy of a Zr-based bulk metallic glass manufactured via laser powder-bed fusion, Materials & Design (2020) 109400. https://doi.org/10.1016/j.matdes.2020.109400.
[12] J.P. Best, H.E. Ostergaard, B. Li, M. Stolpe, F. Yang, K. Nomoto, M.T. Hasib, O. Muránsky, R. Busch, X. Li, J.J. Kruzic, Fracture and fatigue behaviour of a laser additive manufactured Zr-based bulk metallic glass, Additive Manufacturing 36 (2020) 101416. https://doi.org/10.1016/j.addma.2020.101416.
[13] J. Wegner, M. Frey, R. Busch, S. Kleszczynski, Additive manufacturing of a compliant mechanism using Zr-based bulk metallic glass, Additive Manufacturing Letters 39 (2021) 100019. https://doi.org/10.1016/j.addlet.2021.100019.
[14] V. Pacheco, D. Karlsson, J.J. Marattukalam, M. Stolpe, B. Hjörvarsson, U. Jansson, M. Sahlberg, Thermal stability and crystallization of a Zr-based metallic glass produced by suction casting and selective laser melting, Journal of Alloys and Compounds 825 (2020) 153995. https://doi.org/10.1016/j.jallcom.2020.153995.
[15] A. Ericsson, V. Pacheco, M. Sahlberg, J. Lindwall, H. Hallberg, M. Fisk, Transient nucleation in selective laser melting of Zr-based bulk metallic glass, Materials & Design 195 (2020) 108958. https://doi.org/10.1016/j.matdes.2020.108958.
[16] Z. Yang, R. Al-Mukadam, M. Stolpe, M. Markl, J. Deubener, C. Körner, Isothermal crystallization kinetics of an industrial-grade Zr-based bulk metallic glass, Journal of Non-Crystalline Solids 573 (2021) 121145. https://doi.org/10.1016/j.jnoncrysol.2021.121145.
[17] J. Wegner, M. Frey, S. Kleszczynski, R. Busch, G. Witt, Influence of process gas during powder bed fusion with laser beam of Zr-based bulk metallic glasses, Procedia CIRP 94 (2020) 205–210. https://doi.org/10.1016/j.procir.2020.09.039.
[18] J.P. Oliveira, A.D. LaLonde, J. Ma, Processing parameters in laser

powder bed fusion metal additive manufacturing, Materials & Design 193 (2020) 108762. https://doi.org/10.1016/j.matdes.2020.108762.
[19] J.P. Best, K. Nomoto, F. Yang, B. Li, M. Stolpe, L. Zeng, Z. Evenson, C. Hugenschmidt, X. Li, S.P. Ringer, J.J. Kruzic, Advanced structural analysis of a laser additive manufactured Zr-based bulk metallic glass along the build height, J Mater Sci 109 (2022) 375. https://doi.org/10.1007/s10853-022-06991-6.
[20] J. Hwang, Z.H. Melgarejo, Y.E. Kalay, I. Kalay, M.J. Kramer, D.S. Stone, P.M. Voyles, Nanoscale structure and structural relaxation in Zr50Cu45Al5 bulk metallic glass, Physical review letters 108 (2012) 195505. https://doi.org/10.1103/PhysRevLett.108.195505.
[21] K. Nomoto, A.V. Ceguerra, C. Gammer, B. Li, H. Bilal, A. Hohenwarter, B. Gludovatz, J. Eckert, S.P. Ringer, J.J. Kruzic, Medium-range order dictates local hardness in bulk metallic glasses, Materials Today 44 (2021) 48–57. https://doi.org/10.1016/j.mattod.2020.10.032.
[22] L.C. Wei, L.E. Ehrlich, M.J. Powell-Palm, C. Montgomery, J. Beuth, J.A. Malen, Thermal conductivity of metal powders for powder bed additive manufacturing, Additive Manufacturing 21 (2018) 201–208. https://doi.org/10.1016/j.addma.2018.02.002.
[23] B. Cheng, B. Lane, J. Whiting, K. Chou, A Combined Experimental-Numerical Method to Evaluate Powder Thermal Properties in Laser Powder Bed Fusion, J. Manuf. Sci. Eng 140 (2018). https://doi.org/10.1115/1.4040877.
[24] G. Strano, L. Hao, R.M. Everson, K.E. Evans, Surface roughness analysis, modelling and prediction in selective laser melting, Journal of Materials Processing Technology 213 (2013) 589–597. https://doi.org/10.1016/j.jmatprotec.2012.11.011.
[25] J.C. Fox, S.P. Moylan, B.M. Lane, Effect of Process Parameters on the Surface Roughness of Overhanging Structures in Laser Powder Bed Fusion Additive Manufacturing, Procedia CIRP 45 (2016) 131–134. https://doi.org/10.1016/j.procir.2016.02.347.
[26] H. Chen, D. Gu, J. Xiong, M. Xia, Improving additive manufacturing processability of hard-to-process overhanging structure by selective laser melting, Journal of Materials Processing Technology 250 (2017) 99–108. https://doi.org/10.1016/j.jmatprotec.2017.06.044.
[27] P.A. Hooper, Melt pool temperature and cooling rates in laser powder bed fusion, Additive Manufacturing 22 (2018) 548–559. https://doi.org/10.1016/j.addma.2018.05.032.
[28] EOS GmbH, EOS M 100 Datasheet: Additive Manufacturing System for the Fast and Efficient Production of Delicate Metal Parts, 2022, https://www.eos.info/03_system-related-assets/system-related-contents/_pdf_system-data-sheets/eos_system_data_sheet_eos_m_100_en.pdf, accessed 23 May 2022.
[29] N. Schnell, M. Schoeler, G. Witt, S. Kleszczynski, Experimental and numerical thermal analysis of the laser powder bed fusion process using in situ temperature measurements of geometric primitives, Materials & Design 209 (2021) 109946. https://doi.org/10.1016/j.matdes.2021.109946.
[30] D. Kotzem, S. Kleszczynski, F. Stern, A. Elspaß, J. Tenkamp, G. Witt, F. Walther, Impact of single structural voids on fatigue properties of AISI 316L manufactured by laser powder bed fusion, International Journal of Fatigue 148 (2021) 106207. https://doi.org/10.1016/j.ijfatigue.2021.106207.
[31] D. de Moraes, A. Czekanski, Parametric Thermal FE Analysis on the Laser Power Input and Powder Effective Thermal Conductivity during Selective Laser Melting of SS304L, JMMP 2 (2018) 47. https://doi.org/10.3390/jmmp2030047.
[32] Heraeus Additive Manufacturing GmbH, Metal Powder AMZ4 Data sheet, 2018, accessed 11 July 2019.
[33] J. Lindwall, Modelling of Bulk Metallic Glass formation in Powder Bed Fusion, 2019.